Numerical simulation of concrete based modular solid thermal energy storage system

Sarad BASNET[1*], Alix UNTRAU[1], Sonia CARREIRA FERREIRA[2], Sylvain SERRA[1]

[1]Universite de Pau et des Pays de l'Adour, LaTEP, Pau, France
[2]TotalEnergies OneTech, Centre Scientifique et Technique Jean Féger (CSTJF), Avenue Larribau, Pau Cédex 64018, France
[*](Corresponding author: sbasnet@univ-pau.fr)

Abstract—This study presents a hybrid 1D-fluid and 2D-solid numerical model for a solid concrete-based thermal energy storage system. Sensitivity analysis identifies the trade-off for temporal and spatial discretization parameters, maintaining errors below 5%, while physical prevalidation confirms precise thermal gradients and inertia during consecutive 4-hour charge and discharge cycles throughout the 24-hour time horizon. This evaluated framework provides a basis for optimizing future operating strategies to maximize energy use and benefit from grid price variability.

Nomenclature

Latin symbols

A	area, m^2
c_p	specific heat capacity, $\mathrm{J \cdot kg^{-1} \cdot K^{-1}}$
d	diameter, mm
h	convective heat transfer coefficient, $\mathrm{W \cdot m^{-2} \cdot K^{-1}}$
L	effective length, m
$\dot{m}$	mass flow rate, $\mathrm{kg \cdot s^{-1}}$
P	perimeter, m
r	radial coordinate, m
R	radius, mm
t	time, s
T	temperature, $^\circ\mathrm{C}$ or K
u	velocity, $\mathrm{m \cdot s^{-1}}$
x	axial coordinate, m

Greek symbols

λ	thermal conductivity, $\mathrm{W \cdot m^{-1} \cdot K^{-1}}$
μ	dynamic viscosity, $\mathrm{Pa \cdot s}$
ρ	density, $\mathrm{kg \cdot m^{-3}}$

Index and exponent

cte	initial at $t = 0$
eff	effective
f	fluid
fs	fluid-solid interface
in	inlet / inner
out	outlet / outer
s	solid
$tube$	pipe/tube

1. Introduction

The integration of high-temperature Thermal Energy Storage (TES) systems into industrial processes offers a promising solution to enhance energy flexibility and decarbonize heat supply. By acting as a thermal buffer, TES bridges a gap between energy supply and demand, a critical capability for both industrial applications and renewable energy integration. High-temperature TES systems, capable of operating above 400°C, are particularly valuable for electric power generation and high-grade industrial heating. Historically, these temperatures are achieved primarily in Concentrating Solar Power (CSP) plants [1, 2], where the integration of TES significantly enhances operational flexibility. Recent studies indicate a growing interest in solid-based TES, particularly concrete-based systems, due to their cost-effectiveness, durability, and thermal stability. Salomoni et al. [2] established guidelines for designing concrete storage modules integrated with solar fields and Organic Rankine Cycle

https://doi.org/10.25855/SFT2026-122

(ORC) systems. Their work provided simplified procedures for initial sizing and advanced simulation techniques using the Finite Element Method (FEM). Similarly, Doretti et al. [3] introduced a lumped capacitance-based model for the thermal analysis of concrete storage over time. They validated this simulation code against experimental data from a parallelepiped concrete module using mineral oil as the working fluid, underscoring the need for practical prediction tools for real-time applications. Furthermore, Hoivik et al. [4] demonstrated the long-term feasibility of concrete-like materials (e.g., HEATCRETE® vp1) for high-temperature storage. Their analysis of performance data collected over 20 months validated numerical predictions and confirmed the robust performance and material stability of modular concrete systems under various operational modes. While extensive research has been conducted on solid concrete-based TES, a persistent challenge in numerical modeling remains the trade-off between predictive accuracy and computational efficiency. 1D models are simple, while 3D models are computationally costly for extensive analysis. To bridge this gap, we propose a hybrid 1D-fluid/2D-solid approach applied to a high-temperature system (EnergyNest® [4]) coupled with an electric heater. A distinct novelty of this work lies in the implementation of the model within the Pyomo optimization framework solved via the IPOPT solver. This environment is adapted for optimization, facilitating an efficient transition to the dynamic optimization and control strategies. Consequently, while the ultimate goal is to optimize system operation under variable market prices, this specific study concentrates on establishing and validating this optimization-ready numerical framework. Here, we present a dynamic model with rigorous sensitivity analysis on spatial/temporal discretization points and validation of the model with standard charge/discharge cycles throughout the 24-hour time horizon to demonstrate both computational efficiency and physical accuracy.

2. Material and method

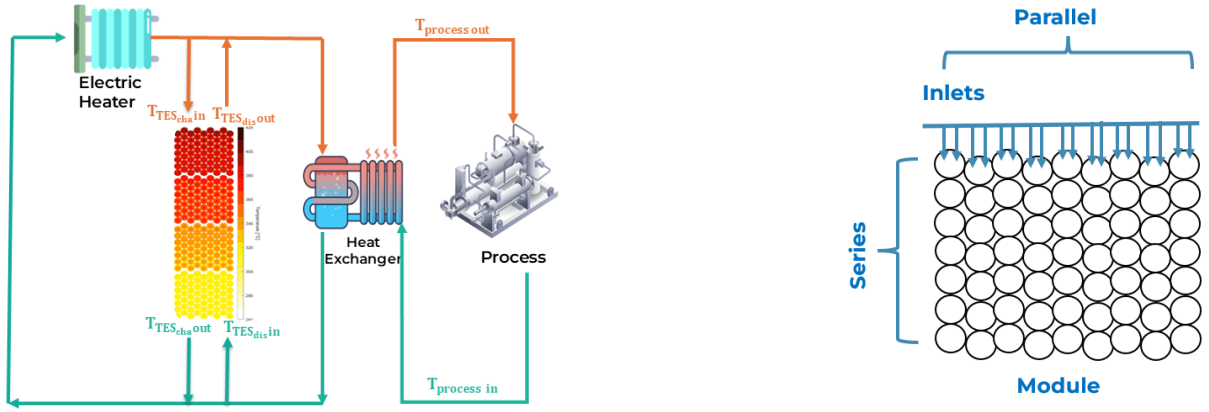

(a) Process Scheme (b) Module Geometry

Figure 1: TES system and concrete storage module topology.

The system architecture, illustrated in Figure 1(a), integrates the thermal storage unit within an industrial process loop. In this configuration, the electric heater, driven by grid electricity subject to variable pricing, primarily ensures that the heat transfer fluid (HTF) reaches the required temperature to satisfy the process heat demand. Consequently, the system supports multiple operating modes: the heater can supply energy directly to the process via the heat exchanger, divert energy to charge the storage module for future use during periods of low electricity prices, or allow the storage to discharge and supply the load during peak pricing intervals. This study focuses primarily on the modeling and simulation of the modular storage unit. The TES unit comprises cylinders with dimensions presented in Figure 2 made of a solid concrete storage medium (HEATCRETE® vp1) [4], integrating tubular

structures within each cylinder configured such that the HTF (Therminol® VP-1 [5]) flows through two parallel U-shaped tubes entering at the inlet during charging. These cylinders are aggregated into thermal modules, where seven cylinders are connected in series to form a single 35 m setup and nine cylinders are connected in parallel. The system integrates 63 cylinders per module and 378 cylinders in total to satisfy the industrial process requirements. The system evaluated in this study utilizes a 3 (series) × 2 (parallel) topology, which consists of two parallel modules, each comprising three modules connected in series. The total length of cylinders in series is thus 105 m (3 modules × 35 m/module). Due to the internal U-tube configuration within each cylinder, the fluid must complete both an outbound and return journey, resulting in a total effective travel length of 210 m per branch.

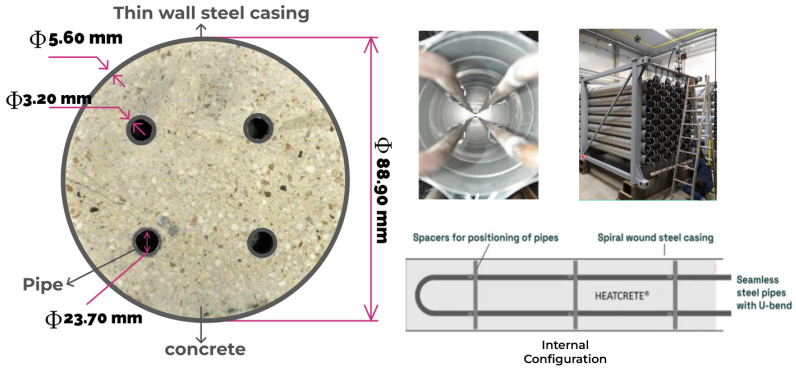

Figure 2: Details of the modular storage unit: Cylinder and tube dimensions [4].

2.1. Assumptions

To reduce modeling complexity, the U-tubes inside all cylinders in series and the manifolds connecting the cylinders are approximated as a continuous linear tube as presented in Figure 3, with a total length of 210 m as explained in the previous paragraph. The cylindrical concrete domain is partitioned into four identical quadrants, each containing one pipe. Each quadrant is assimilated to a 2D axial-radial (x, r) domain as presented in Figure 3. Due to the symmetry between the two U-shaped tubes, only one half of the cylinder is modeled. This domain includes both the outbound and return sections of a single U-shaped tube, thereby representing the full length of a U-shaped tube. It is further assumed that there is no heat exchange between the solid regions surrounding the inbound and return pipes. Parallel branches are not explicitly modeled, assuming uniform flow and heat transfer across the module. An assumption of uniform distribution of flow through the 36 parallel pathways is made. The rationale for this assumption can be attributed to the fact that there is uniformity in the geometry of the tubes coupled with their interconnection through common manifolds, which leads to uniformity in pressure drop between the modules. Consequently, edge effects are neglected, and heat losses to the ambient are not considered, allowing both interior and edge cylinders to be modeled in the same manner.

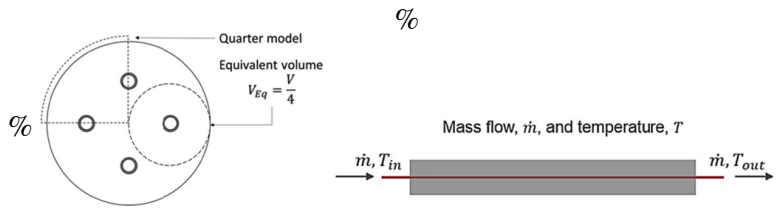

Figure 3: Assumed long tube and quarter model derived from [4].

2.2. Parameters

The thermophysical properties of the solid storage medium (HEATCRETE® vp1) and the heat transfer fluid (Therminol® VP-1), along with the geometric and fluid parameters governing the sim-

ulation, are summarized in Table 1. Although the thermophysical properties of the materials exhibit temperature dependence, they are treated as constant parameters in this study. To accurately approximate material behavior across the operating range of 230.5°C to 390.0°C, all property values were generated at the temperature of 350°C [6]. A comparative analysis confirms that despite significant thermophysical variations in Therminol® VP-1 across the operating range from 390°C to 230.5°C (e.g., a 18% decrease in density), the relative errors in temperatures and energy remain below 1.5% which is negligible. Consequently, the constant property approach provides a high-fidelity, time-efficient approximation for system optimization.

Parameter	Symbol	Value	Unit
Fluid Properties (Therminol ®VP-1) [5]			
Density	ρ_f	769.97	$\mathrm{kg \cdot m^{-3}}$
Specific Heat Capacity	$c_{p,f}$	2334.84	$\mathrm{J \cdot kg^{-1} \cdot K^{-1}}$
Thermal Conductivity	λ_f	0.0864	$\mathrm{W \cdot m^{-1} \cdot K^{-1}}$
Dynamic Viscosity	μ_f	1.77×10^{-4}	$\mathrm{Pa \cdot s}$
Solid Properties (HEATCRETE® vp1) [4]			
Density	ρ_s	2366.0	$\mathrm{kg \cdot m^{-3}}$
Specific Heat Capacity	$c_{p,s}$	1025.0	$\mathrm{J \cdot kg^{-1} \cdot K^{-1}}$
Thermal Conductivity	λ_s	1.92	$\mathrm{W \cdot m^{-1} \cdot K^{-1}}$
Geometric and Flow Parameters			
Tube Inner Diameter	d_{tube}	23.7	mm
Total Effective Length	L	210.0	m
Flow Area	A_f	4.4×10^{-4}	$\mathrm{m^2}$
Mass Flow Rate	$\dot{m}$	0.33	$\mathrm{kg \cdot s^{-1}}$
Fluid Velocity	u	0.6	$\mathrm{m \cdot s^{-1}}$
Convective Coeff.	h	1582.82	$\mathrm{W \cdot m^{-2} \cdot K^{-1}}$

Table 1: Thermophysical properties and simulation parameters.

2.3. Governing Equations

The heat transfer within the fluid domain is governed by the 1D advection-diffusion equation, incorporating an axial flow term and a source term representing the convective heat exchange of fluid with the solid wall. The energy balance for the fluid is given by:

$$\rho_f c_{p,f} \frac{\partial T_f}{\partial t} = -\rho_f c_{p,f} u_f(t) \frac{\partial T_f}{\partial x} + \lambda_f \frac{\partial^2 T_f}{\partial x^2} + h_{fs} \frac{P_{tube}}{A_{tube}} (T_s|_{r=R_{in}} - T_f) \tag{1}$$

The solid storage material is modeled using the 2D transient heat conduction equation in cylindrical coordinates, accounting for both axial and radial diffusion:

$$\rho_s c_{p,s} \frac{\partial T_s}{\partial t} = \lambda_s \left[\frac{\partial^2 T_s}{\partial x^2} + \frac{1}{r} \frac{\partial}{\partial r} \left(r \frac{\partial T_s}{\partial r} \right) \right] \tag{2}$$

2.4. Boundary Conditions and Numerical Implementation

The system operates in a cyclic manner with a charge period ($u_f > 0$) and a discharge period ($u_f < 0$). The fluid boundary conditions, presented in Eq. 3, switch dynamically based on the flow direction. During the charging phase, a Dirichlet condition (390°C) is applied at the inlet ($x = 0$), while a Neumann condition is applied at the outlet ($x = L$) to represent fully developed outflow (zero thermal gradient). Conversely, during the discharging phase, the flow reverses; the inlet shifts to $x = L$ with the baseline temperature (230.5°C), and the adiabatic Neumann condition is applied at $x = 0$.

$$Charge(u_f > 0): \quad T_f(0,t) = T_{charge}; \quad \left.\frac{\partial T_f}{\partial x}\right|_L = 0 \tag{3a}$$

$$Discharge(u_f < 0): \quad T_f(L,t) = T_{discharge}; \quad \left.\frac{\partial T_f}{\partial x}\right|_0 = 0 \tag{3b}$$

$$InitialCond.: \quad T_f(x,0) = T_{cte} = 230.5°\mathrm{C} \tag{3c}$$

The system is configured so that charging and discharging do not occur simultaneously. The Neumann boundary condition, $\partial T_f / \partial x = 0$, used for simulating the complete development of the thermal flow, is switched depending on operating charging and discharging modes from the position $x = L$ to $x = 0$ during the cycle. Although this creates a numerical constraint on the fixed length of $L = 210$ m, the

physical accuracy of the simulation is preserved through the strong advection ($u_f = 0.97$ m/s) and the large overall length of the system. This ensures that the axial gradient of temperature reduces naturally near the exit point, thereby avoiding any unphysical deviation of the temperature distribution or the fixed heat transfer coefficient. For the solid domain, the boundary conditions in Eq. 4 describe the convective heat exchange at the inner fluid-solid interface, the adiabatic insulation at the outer walls and cylinder ends where heat losses to the ambient are neglected, and the initial thermal equilibrium state:

$$r = R_{in}: \quad \lambda_s \frac{\partial T_s}{\partial r}\bigg|_{R_{in}} = h_{fs}(T_s - T_f) \qquad \text{(Robin: Coupling)} \tag{4a}$$

$$r = R_{out}: \quad \frac{\partial T_s}{\partial r}\bigg|_{R_{out}} = 0 \qquad \text{(Adiabatic Wall)} \tag{4b}$$

$$x = \{0, L\}: \quad \frac{\partial T_s}{\partial x} = 0 \qquad \text{(Adiabatic Ends)} \tag{4c}$$

$$t = 0: \quad T_s(x, r, 0) = T_{cte} = 230.5^{\circ}\text{C} \qquad \text{(Solid Initial Cond.)} \tag{4d}$$

2.5. Discretization and Resolution Method

The transient energy conservation equations are discretized using the Finite Difference Method (FDM) with a fully implicit Backward Euler time integration scheme to ensure numerical stability. Spatially, the formulation adopts a central difference approach for second-order diffusion terms in both axial (x) and radial (r) directions, while the fluid advection term utilizes a first-order upwind scheme to properly manage flow directionality. Accordingly, the discretized governing equation for a general computational node at time step t, axial location x, and radial coordinate r is approximated as shown in Equation 5.

$$\rho c_p \frac{T^t_{x,r} - T^{t-1}_{x,r}}{\Delta t} + \underbrace{\rho c_p u \frac{T^t_{x,r} - T^t_{x-\Delta x,r}}{\Delta x}}_{\text{Fluid Advection (Backward)}} = \underbrace{\lambda \left[\frac{T^t_{x+\Delta x,r} - 2T^t_{x,r} + T^t_{x-\Delta x,r}}{\Delta x^2} + \dots \right]}_{\text{Diffusion (Central)}} + S_{x,r} \tag{5}$$

where $S_{x,r}$ represents the convective heat transfer towards the solid. In the fluid domain ($u \neq 0$), the radial diffusion component is omitted, reducing the formulation to a 1D model. Conversely, in the solid domain ($u = 0$), the advection term vanishes, and the standard central difference scheme is applied to the radial conduction term ($\frac{1}{r}\frac{\partial}{\partial r}(r\frac{\partial T}{\partial r})$). The model is implemented in Python using the Pyomo framework [7] and solved via IPOPT. While Pyomo.DAE handles temporal discretization; spatial PDEs are manually discretized to bypass the framework's limitations with second-order derivatives. This explicit formulation enables the flexibility to apply the conditional upwind scheme required for cyclic charge and discharge operations.

3. Results and Discussion

3.1. Numerical Verification

Case	N_x	N_r	N_t	Energy Norm. Error (%)	Fluid Temp. Rel. Error (%)	Solid Temp. Rel. Error (%)	Solver Time (s)
Axial Sensitivity (Fixed $N_r = 10, N_t = 24$***)***							
Coarse	2	10	24	5.84	1.23	1.16	0.84
Fine	30	10	24	0.55	0.04	0.04	64.10
Selected N_x	**20**	**10**	**24**	**1.23**	**0.09**	**0.09**	**32.04**
Radial Sensitivity (Fixed $N_x = 20, N_t = 24$***)***							
Coarse	20	2	24	25.60	20.77	20.56	2.01
Fine	20	15	24	0.81	0.85	0.87	87.41
Selected N_r	**20**	**10**	**24**	**2.46**	**2.57**	**2.61**	**31.72**
Temporal Sensitivity (Fixed $N_x = 20, N_r = 10$***)***							
Coarse	20	10	24	16.20	8.67	8.80	32.89
Fine	20	10	144	3.15	2.83	0.95	312.92
Selected N_t	**20**	**10**	**144**	**3.15**	**2.83**	**0.95**	**312.92**

Table 2: Grid and time step sensitivity analysis results.
(Rel.: Relative Error, Norm.: Normalized Error)

To optimize computational efficiency without compromising accuracy, a stepwise sensitivity analysis was conducted by refining the axial (N_x), radial (N_r), and temporal (N_t) discretization parameters.

The deviations in fluid temperature (evaluated at x_{in}), solid temperature (evaluated at x_{in}, r_{in}), and stored energy were compared against a high-resolution benchmark ($N_x = 50, N_r = 20, N_t = 288$), as summarized in Table 2. The reported energy error represents the mean absolute deviation over the 24-hour cycle, normalized with respect to the maximum energy stored. The model demonstrated low sensitivity to axial resolution; increasing N_x from 2 to 30 reduced the normalized energy error from 5.84% to 0.55%, though it increased solver time from 0.84 s to 64.10 s. The selected value $N_x = 20$ offered a good trade-off, maintaining a mean normalized energy error of 1.23% over the time and a negligible 0.09% mean relative error in temperature profiles. Conversely, the system proved highly sensitive to radial discretization due to thermal gradients within the solid. While a coarse mesh ($N_r = 2$) resulted in errors exceeding 20%, increasing the resolution to $N_r = 10$ reduced the relative error to $\approx 2.5\%$, providing acceptable accuracy at a significantly lower computational cost (31.72 s) compared to the finer mesh ($N_r = 15$, 87.41 s). Finally, capturing transient dynamics required finer temporal steps. Refining the discretization from $N_t = 24$ (1-hour step) to $N_t = 144$ (10-minute step) drastically improved performance, reducing mean fluid and solid temperature errors $\approx 8.5\%$ to below 5%. The computational cost of the selected configuration ($N_x = 20, N_r = 10, N_t = 144$) was approximately 5.2 minutes (312.92 s). This represents a substantial gain in efficiency compared to higher-fidelity benchmarks: a configuration of $N_x = 30, N_r = 10, N_t = 288$ required approximately 33 minutes, while increasing radial precision further ($N_r = 15$) extended the simulation time to 88.24 minutes. Consequently, the selected discretization points achieve a speedup factor of 6 to 17 while maintaining all relative errors strictly below the 5% threshold, confirming their suitability for extensive optimization tasks.

3.2. Physical model prevalidation

Following the computations using the spatial and temporal discretization points, the model was evaluated by simulating one complete 24-hour operation sequence consisting of alternating charge and discharge cycles, each lasting 4 hours, as depicted in Figure 4. This section presents the physical evaluation of the system, which depicts the thermodynamic behavior of both the HTF and solid concrete medium. The spatial temperature distribution is presented for both the fluid and solid domains to ensure that the heat exchange mechanisms are appropriately captured under cyclic operation. The

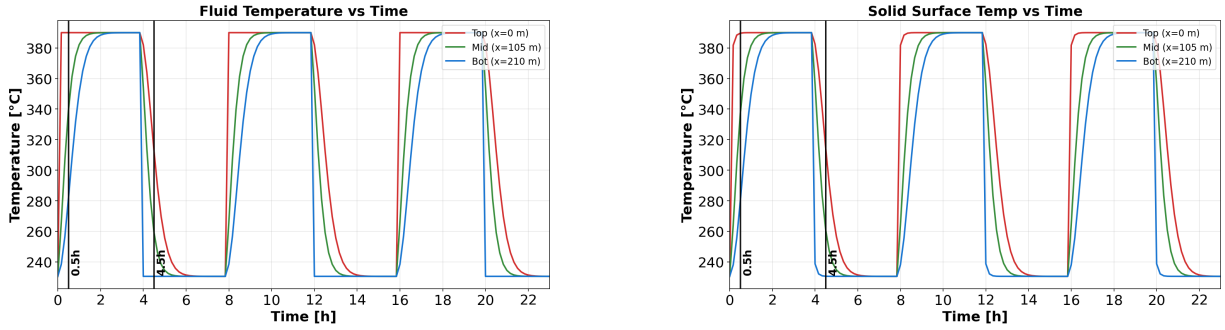

(a) Fluid temperature

(b) Solid temperature

Figure 4: Transient temperature evolution at the inlet, midpoint, and outlet of the tube.

transient system response is plotted for three consecutive periods of 8 hours. During the first 4-hour charging, hot fluid at 390°C enters through the inlet at the top of the storage. As can be observed from Figure 4, the temperature rises almost instantaneously at the inlet, while the profiles at the mid-height and bottom locations show a characteristic time lag. This delay corresponds to the physical time required for the hot fluid to travel the entire length of the tube and increase the temperature of the solid, as the fluid must first transfer its energy to the upstream sections before heating the downstream locations. In the subsequent discharge phase, occurring from the fourth to the eighth hour, the flow

direction reverses, and cold fluid at 230.5°C is injected at the bottom of the storage, which becomes the new inlet. Consequently, the temperature at the bottom drops first to 230.5°C, followed sequentially by the middle and top sections (outlet). Comparing the fluid and solid responses in Figures 4(a) and 4(b), the solid surface temperature closely follows the fluid profile but exhibits a distinct time lag. This delay confirms that the model quantitatively captures the thermal inertia of the concrete storage medium, reflecting the time required for heat to transfer from the fluid interface into the solid material.

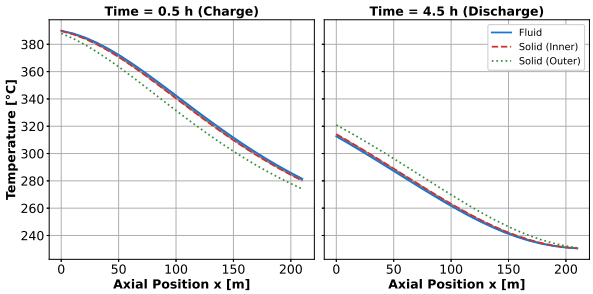

(a) Axial fluid and solid temperature profiles

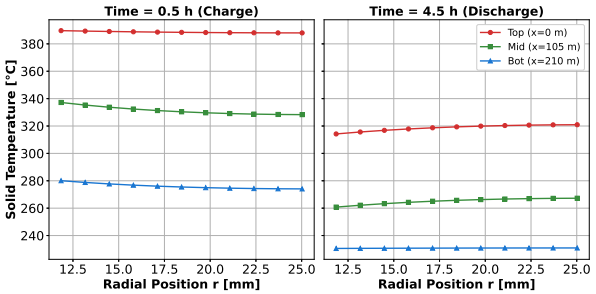

(b) Radial solid temperature profiles

Figure 5: Spatial temperature evolution along the length and radius of a tube.

To further analyze and evaluate the physical model, the fluid and solid temperatures were examined along the length of the tube and across the thickness of the concrete cylinder. This analysis was performed at two specific moments indicated by the black vertical lines in Figure 4: thirty minutes into the charging cycle, when hot fluid flows from the top, and thirty minutes into the discharging cycle, when cold fluid flows from the bottom. The results confirm that heat flows in the correct direction based on the temperature differences. Figure 5(a) displays the temperature profiles for the fluid, at the solid inner radius (where the fluid interacts with the solid), and at the solid outer radius. During the charging phase, the fluid is consistently hotter than the solid material, which drives heat from the fluid into the storage medium. Due to the direct heat exchange, the inner radius of solid which is close to the fluid, closely tracks the fluid temperature, albeit with a slight thermal lag, while the outer radius maintains a lower temperature than the inner radius. In contrast, during the discharge phase, the flow reverses and cold fluid enters the system. Under these conditions, the thermal gradient flips: the outer radius becomes hotter than the inner radius, and both are hotter than the fluid. This effectively releases stored energy from the bulk concrete back into the fluid stream. The radial temperature distribution, shown in Figure 5(b), further depicts this mechanism. The profiles exhibit a nearly linear trend with moderate gradients in the radial direction for various axial points, attributed to the storage medium's relatively small thickness. The temperature profiles exhibit a nearly linear trend with moderate radial gradients at various axial points, which is attributed to the relatively small thickness of the concrete medium. The Biot's number (Bi :5–11), being significantly greater than one, indicates that the convective resistance at the fluid–solid interface is small compared to the internal conduction resistance within the solid. As a result, heat is transferred efficiently at the surface, while temperature gradients develop within the solid, governed primarily by its radial diffusion. During charging, temperatures decrease from the inner to the outer radius, indicating outward heat diffusion. Conversely, during discharge, the rapid cooling of the inner surface reverses this slope; the outer radius remains hotter, driving heat from the concrete core back toward the fluid interface.

After the validation of the spatial distributions of temperatures, the overall performance of the system is assessed by tracking the State of Charge (SOC), which is the percentage of the total theoretical capacity (1.24 MWh) available in the concrete material. Figure 6 shows the time evolution of the SOC through one day, which comprises three charge-discharge cycles. It clearly presents a periodic pattern, indicating that the stability condition is reached successfully in our case study. During the

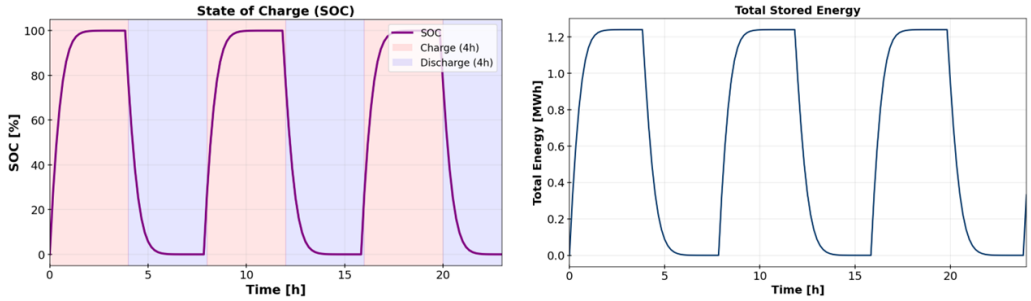

Figure 6: Cyclic variation of the State of Charge (SOC) and energy throughout a 24-hour operation period.

charge process (red-shaded area), the SOC grows due to the heating of the upstream units to the set temperature of 390°C. The SOC reaches its maximum of 100% which means that the front of the battery system is charged up to 100%.

4. Conclusion

This study developed and evaluated a computationally efficient hybrid 1D-fluid and 2D-solid numerical model for a concrete-based TES system. Through a rigorous sensitivity analysis, an optimal discretization scheme was identified ($N_x = 20, N_r = 10, N_t = 144$) that maintains relative errors below 5% while minimizing computational cost. Physical prevalidation further confirmed the model's thermodynamic consistency, quantitatively capturing radial thermal gradients, thermal inertia, and stable cyclic behavior. With the numerical framework established, the immediate future work focuses on validating the model against experimental data. One of the perspectives in the next stage will be that of improving the model for practical applications by integrating a global heat loss term. This extension will allow for a precise assessment of long-term State of Charge (SOC) drift and the symmetry of thermal fronts in real-world environments. Following this confirmation, the model is prepared to be extended into its intended application: identifying optimal operating strategies over a time horizon to maximize energy utilization and benefit from grid price variability.

References

[1] Doerte Laing, Wolf-Dieter Steinmann, Rainer Tamme, and Christoph Richter. Solid media thermal storage for parabolic trough power plants. *Solar energy*, 80(10):1283–1289, 2006.

[2] Valentina A Salomoni, Carmelo E Majorana, Giuseppe M Giannuzzi, Adio Miliozzi, Rosa Di Maggio, Fabrizio Girardi, Domenico Mele, and Marco Lucentini. Thermal storage of sensible heat using concrete modules in solar power plants. *Solar Energy*, 103:303–315, 2014.

[3] Luca Doretti, Francesca Martelletto, and Simone Mancin. A simplified analytical approach for concrete sensible thermal energy storages simulation. *Journal of Energy Storage*, 22:68–79, 2019.

[4] Nils Hoivik, Christopher Greiner, Juan Barragan, Alberto Crespo Iniesta, Geir Skeie, Pål Bergan, Pablo Blanco-Rodriguez, and Nicolas Calvet. Long-term performance results of concrete-based modular thermal energy storage system. *Journal of Energy Storage*, 24:100735, 2019.

[5] Therminol® heat transfer fluids, 2026. Accessed: 2026-01-06.

[6] Reuben Buehler, Sam Yang, and Juan C. Ordonez. Heat transfer fluids for parabolic trough solar collectors - a comparative study. In *2016 IEEE Conference on Technologies for Sustainability (SusTech)*, pages 68–75, 2016.

[7] Michael L Bynum, Gabriel A Hackebeil, William E Hart, Carl D Laird, Bethany L Nicholson, John D Siirola, Jean-Paul Watson, David L Woodruff, et al. *Pyomo-optimization modeling in python*, volume 67. Springer, 2021.